

First-principle event reconstruction by time-charge readouts for the Taishan Antineutrino Observatory

Xuwei Liu^{1,2,3}, Wei Dou^{1,2,3}, Benda Xu^{1,2,3,4}, Hanwen Wang⁵, and Guofu Cao⁵

¹ Department of Engineering Physics, Tsinghua University, Beijing, China

² Center for High Energy Physics, Tsinghua University, Beijing, China

³ Key Laboratory of Particle & Radiation Imaging (Tsinghua University), Ministry of Education, China

⁴ Kavli Institute for the Physics and Mathematics of the Universe, UTIAS, the University of Tokyo, Tokyo, Japan

⁵ Institute of High Energy Physics, Chinese Academy of Sciences, Beijing, China

Received: date / Revised version: date

Abstract. The Taishan Antineutrino Observatory (TAO) is a liquid-scintillator satellite experiment of the Jiangmen Underground Neutrino Observatory (JUNO) to measure the reference reactor neutrino spectrum with unprecedented energy resolution. We use inhomogeneous Poisson process and Tweedie generalized linear model (GLM) to characterize the detector response and the charge distribution of a SiPM. We develop a pure probabilistic model for time and charge of SiPMs from first principles to reconstruct point-like events in the TAO central detector. Thanks to our precise model and the high photo-coverage and quantum efficiency of the SiPM tiles at TAO, we achieve vertex position resolution better than 20 mm, energy resolution of about 2% at 1 MeV and <0.5% non-uniformity, marking the world's best performance of liquid scintillator detectors. With such resolution, we perceive MeV events to exhibit track effects. It opens up an exciting possibility of computed tracking calorimeter for unsegmented liquid scintillator detector like TAO. Our methodology is applicable to other experiments that utilize PMTs for time and charge readouts.

PACS. XX.XX.XX No PACS code given

1 Introduction

The Taishan Antineutrino Observatory (TAO) is a satellite experiment of the Jiangmen Underground Neutrino Observatory (JUNO) [1]. Using 2.8 tons Gadolinium-doped Liquid Scintillator (GdLS) and 4024 Silicon Photomultiplier (SiPM) tiles, TAO will measure the neutrino energy spectrum with unprecedented precision from a reactor core of the Taishan Nuclear Power Plant 44 m away. The neutrino energy spectra predicted from recent computations [2,3] disagree with the ones measured by the previous reactor neutrino experiments such as Daya Bay [4], Double Chooz [5], RENO [6], NEOS [7], STEREO [8]. The inconsistency is believed to have its roots in lack of complete information on decay and fission yields from the nuclear database [9]. To determine the neutrino mass ordering, JUNO demands TAO for model-independent reference spectra [10]. The TAO collaboration plans to benchmark the nuclear database with fine structures in the antineutrino spectra [11]. Thus, we require the position resolution to be better than 5 cm, energy resolution to be $\sim 2\%$ at 1 MeV and energy non-uniformity to be contained within 0.5% after *event reconstruction* [1,12].

In many large liquid scintillation and water Cherenkov detectors, the arrival time of the first photoelectron (PE) and the total integrated charge in a chunk of PMT/SiPM readout waveforms are input to the event reconstruction stage of data reduction. The time distribution of the first PE is long known to be affected by PE pile-up [13,14]. KamLAND [15] uses a time-only vertex fitter with heuristic corrections. Borexino [16] and Super-Kamiokande [17] construct several empirical first-PE time probability density functions (PDF) from both calibration and Monte Carlo conditioned on charges. Z. Li et al [18] derive a rigorous time dependence on the PE counts for JUNO. However, the counts are inaccurately estimated from rounding charges to integers. G. Huang et al. [19] improve upon it by relying on both the PE count and expectation of it. But the time-charge-combined likelihood is an oversimplified direct product assuming independence of the two components. Such approximations introduce inherent bias needing to be *ad-hocly* corrected *a posteriori* in form of *correction maps*. Z. Qian et al. [20] and Gavrikov et al. [21] discuss the application of several convenient and flexible end-to-end machine learning models, though the performance of which depends on high-fidelity Monte Carlo, selection of aggregated features and optimal hyperparameters. It still needs to be measured and hopefully corrected how much extra non-uniformity an algorithm imposes.

To address those difficulties, a fundamental model derived from first principles is necessary, especially for an experiment like TAO with unprecedented energy and vertex resolution. We use Tweedie generalized linear

model (GLM) to describe the probabilistic relation of PE count and charge. Upon it, we derive an exact joint time-charge PDF from the original light curve. The resulting reconstruction algorithm is free from correction maps and hyperparameters. It is transparent in that the non-uniformity of the reconstructed energy is entirely determined by the detector calibration. Sec. 2 discusses the definition and implementation of the detector response for a point-like event in the TAO central detector. Sec. 3 derives the exact time-charge likelihood from the Tweedie distribution. Sec. 4 introduces the dataset before evaluating the bias and resolution of the reconstructed position and energy. Sec. 5 discusses the limitations of our approach and future improvements. Finally, we conclude in Sec. 6.

2 Optical detector model

Fig. 1 shows the schematic of TAO central detector (CD). A spherical acrylic vessel with an inner diameter of 1.8 m is filled with ~ 2.8 tons GdLS. The fiducial volume expands to the radius of 0.65 m, 0.25 m away from the boundary of acrylic vessel. A total number of 4024 $50.7 \times 50.7 \text{ mm}^2$ SiPM tiles with around fifty percent photon detection efficiency are installed on the inner surface of copper shell supporting the acrylic vessel. The copper shell is immersed in a linear alkylbenzene (LAB) buffer inside a cylindrical stainless-steel tank. We focus on the TAO CD and refer other sub-systems to H. Xu et al. [1] and Abusleme et al. (JUNO collaboration) [12]. TAO detector is under construction and we deploy Monte Carlo (MC) simulation to train the detector response and evaluate the reconstruction algorithm (Sec. 4).

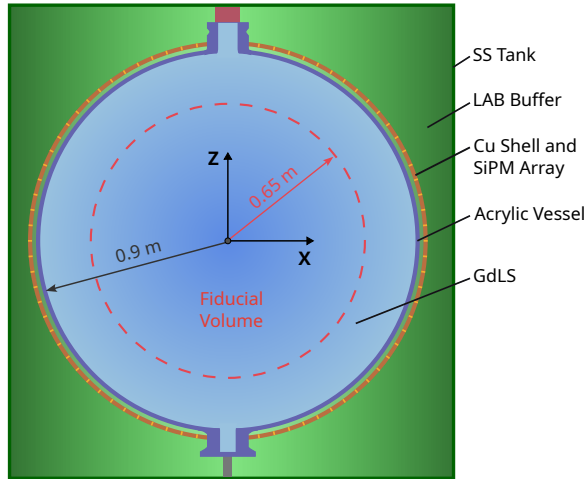


Fig. 1: Schematic of the TAO central detector.

The detector response is defined as a map from a point-like event to the time-charge distributions on SiPM tiles. We divide it into two stages. In this section, the first stage of the response function is optical. It maps an event to PE times for a SiPM, which is properly described by an inhomogeneous Poisson point process. We utilize the approach developed by W. Dou et al. [22] to characterize the optical properties of the detector including the GdLS time profile and photon transmission. The second stage is the electronics. It maps the count and times of the PEs in a SiPM to the first-PE time and the total charge, modeling the SiPM and analog-to-digital system. We shall discuss it in Sec. 3.

2.1 Poisson point process

Consider the response function of a point-like event $\delta(\vec{r}, E)$ on j th SiPM, where \vec{r} and E are the vertex and energy of the event. The occurrence of PE on j th SiPM follows an inhomogeneous Poisson process with intensity function $R_j(t; \vec{r}, E)$ [23]. The PE count on j th SiPM within the time interval $[\underline{T}, \overline{T}]$ follows Poisson distribution (Fig. 2a) of expectation

$$\lambda_{j, [\underline{T}, \overline{T}]}(\vec{r}, E) = \int_{\underline{T}}^{\overline{T}} R_j(t; \vec{r}, E) dt. \quad (1)$$

The ionization quenching and Cherenkov radiation [24] cause the non-linearity between the number of emitted photons and the kinetic energy of the charged particle. Such *physics non-linearity* is usually modeled empirically and calibrated with monoenergetic sources, for example at Daya Bay [24], RENO [25] and Borexino [26]. In the scope of event reconstruction, E is measured in a scale proportional to the number of emitted photons,

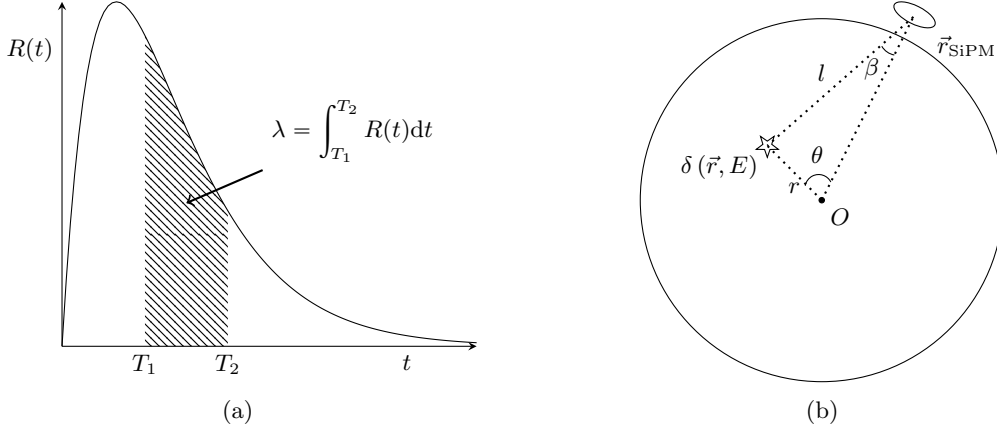


Fig. 2: (a) The physical meaning of response function $R(t)$. The PE count in $[T_1, T_2]$ follows Poisson distribution, and the mean PE count is $\lambda = \int_{T_1}^{T_2} R(t) dt$. (b) The schematic diagram of relative positions (r, θ) of event vertex \vec{r} and SiPM \vec{r}_{SiPM} in CD. β is the incident angle on SiPM. l is the distance from vertex to the position of SiPM. The origin of spherical coordinate system O is put at the center of CD. The detector is approximately symmetric rotationally about the $O-\vec{r}_{\text{SiPM},j}$ axis, thus the relative azimuth ϕ is ignored.

also known as *visible energy*, $v(E)$. Because $v(E)$ describes photon generation, it is decoupled from photon propagation and detection in $R_j(\cdot)$, resulting in separation of variables E and \vec{r} ,

$$R_j(t; \vec{r}, E) = \underbrace{v(E)}_{\text{physics non-linearity}} \cdot \underbrace{R_j^0(t; \vec{r})}_{\text{geometric effect}}. \quad (2)$$

$R_j^0(t; \vec{r})$ encodes *geometric effect*, the relative difference of the light curve over different \vec{r} at the j -th SiPM.

The good spherical symmetry of TAO CD makes the azimuth ϕ irrelevant in the relative position (r, θ, ϕ) between a vertex \vec{r} and position of the j th SiPM $\vec{r}_{\text{SiPM},j}$ (Fig. 2b). After factoring out the quantum efficiency and time difference in the SiPM index j , for a vertex \vec{r}_i , $R_j^0(t; \vec{r}_i)$ merges into a single function $R^0(t; r_i, \theta_{ji})$, where

$$r_i = |\vec{r}_i|, \quad \cos \theta_{ji} = \left(\frac{\vec{r}_i \cdot \vec{r}_{\text{SiPM},j}}{|\vec{r}_i| |\vec{r}_{\text{SiPM},j}|} \right). \quad (3)$$

In TAO, the detector size is much smaller than the scattering or absorption lengths. The variables of $R(t; r, \theta)$ can be separated into time t and position (r, θ) .

2.2 Position part

The response intensity $I(r, \theta) := \int R^0(t; r, \theta) dt$ is defined as the relative PE count on a SiPM tile for given (r, θ) . The accuracy of it dominates the energy non-uniformity of reconstructed events. $I(r, \theta)$ is approximately proportional to the solid angle Ω of SiPM measured from vertex and the exponential attenuation of distance l from vertex to the position of SiPM,

$$I(r, \theta) \propto \Omega \cdot \exp(-l/l_0) \\ \propto \frac{\cos \beta(r, \theta)}{r^2 + r_{\text{SiPM}}^2 - 2rr_{\text{SiPM}} \cos \theta} \cdot \exp(-l/l_0), \quad (4)$$

where $\beta(r, \theta)$ is the incident angle on SiPM shown in Fig. 2b and l_0 is the attenuation length. At TAO, more accuracy in $I(\cdot)$ is needed. We follow W. Dou et al. [22] to characterize the response intensity with Zernike polynomials $Z_n(r, \theta)$ [27] which are orthonormal on the unit disk

$$I(r, \theta) = \Omega \cdot \exp \left[\sum_{n=0}^{N_z} a_n Z_n(r/r_{\text{max}}, \theta) \right], \quad (5)$$

where $r_{\text{max}} = 0.9$ m and N_z is the maximum order. The exponential in Eq. (5) maintains positiveness of the intensity and encodes both the solid angle and the exponential attenuation components in Eq. (4).

$$I'(r, \theta) = \left[\sum_{n=0}^{N_z} a_n Z_n(r/r_{\text{max}}, \theta) \right]^2, \quad (6)$$

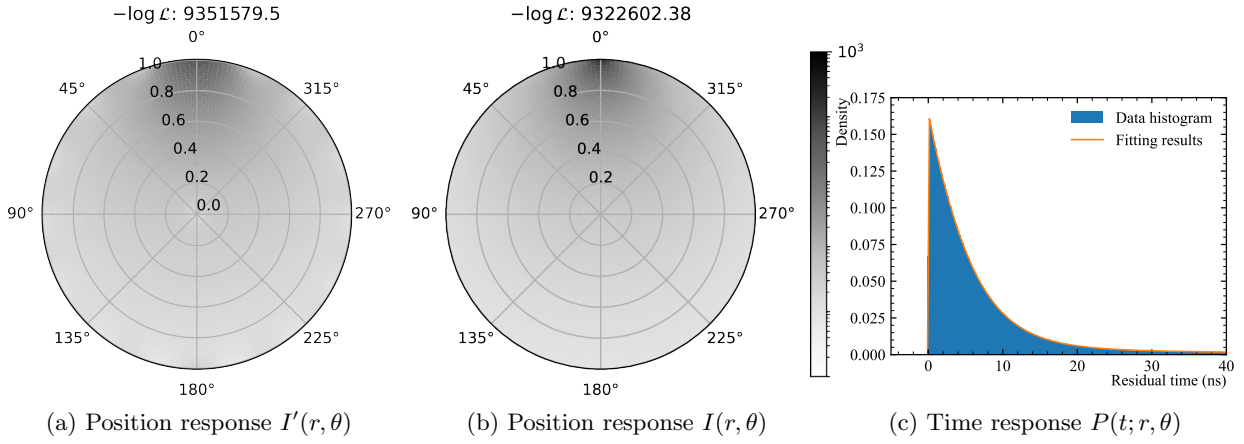


Fig. 3: (a) and (b) show the position response in $I'(r, \theta)$ of square Zernike polynomials and $I(r, \theta)$ of exponential geometrical construction. The score (log-likelihood of the validation dataset) indicates the latter is better. (c) shows time response $P(t; r, \theta)$ fitted by Eq. (9) with 80-order Legendre polynomials. The bin width of histogram is 0.2 ns.

is a radically data-driven form to ensure positiveness.

To decide which form of the position response to use, we fit the same training dataset with Eqs. (6)(5) and use the same validation dataset introduced in Sec. 2.4 to evaluate them. The log-likelihoods and Fig. 3b indicate that the exponential of Zernike polynomials is more suitable for the description of the position response.

2.3 Time part

We set the event times to 0 without loss of generality. The separation of position and time variables implies that the shape of the time response remains consistent across all SiPM tiles and vertices in the CD. To align the arrival times of photons on different SiPM, we define the shift t_{shift} as the time of flight from vertex $\delta(\vec{r}, E)$ to the position of SiPM

$$t_{\text{shift}}(r, \theta) = \frac{n_{\text{LS}} l(r, \theta)}{c}, \quad (7)$$

where n_{LS} is the effective refractive index of liquid scintillator (LS) considering dispersion, l is the distance from vertex to the position of SiPM and c is the speed of light in vacuum. Inspired by Z. Li [18] to determine n_{LS} , we simulate 10,000 5 MeV electrons located at a fixed point and get the peak position of hit time distribution for each SiPM. Fig. 4 shows a 2-D histogram of PE hit times and distances $l(r, \theta)$ on 4024 SiPM tiles. The lower edge of the histogram represents the first-PE time and is linearly fitted to extract n_{LS} .

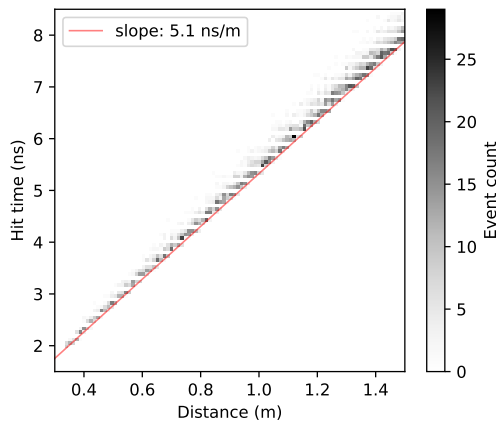


Fig. 4: The histogram of hit times and distances. A linear equation (red line) is used to fit the lower edge of the histogram. The reciprocal of slope is the effective light speed.

The family of Legendre polynomial [28] is orthonormal on $[-1, 1]$. We scale the residual time $t - t_{\text{shift}}$ to $[-1, 1]$ with

$$t_{\text{scale}} = \frac{t - t_{\text{shift}} - \underline{T}}{\overline{T} - \underline{T}} \times 2 - 1, \quad (8)$$

where $[\underline{T}, \overline{T}]$ is the residual time windows including dominant part of time response,

$$P(t; r, \theta) = \exp \left[\sum_{m=0}^{N_p} a_m P_m(t_{\text{scale}}) \right], \quad (9)$$

where $P_m(\cdot)$ is the m -th order Legendre polynomial and N_p is the maximum order. The exponential is to ensure the time part to be nonnegative.

We simulate 100 000 0.5 MeV (kinetic energy) electrons distributed uniformly in CD, calculate the relative positions for all PE hits in Fig. 2b and fit the coefficients a_m in Eq. (9). Fig. 3c shows the fitting results. The residual time window $[\underline{T}, \overline{T}]$ is set to $[-0.5 \text{ ns}, 50 \text{ ns}]$. The time response $P(t)$ outside $[\underline{T}, \overline{T}]$ is considered as zero. The maximum order of Legendre polynomials is determined by an independent validation dataset.

The optical response function is

$$R^0(t; r, \theta) = I(r, \theta) \cdot P(t; r, \theta). \quad (10)$$

2.4 Coefficients fitting and scoring

Electron is an ideal point source in LS because its energy deposition occurs within a radius of a few millimeters [29]. It deposits energy in CD and excites LS molecules. The molecules de-excite and emit scintillation photons, which transmit through the detector and reach the SiPM to produce a PE in part. Those are simulated with GEANT4-based [30] program. In the simulation for coefficients fitting and scoring, 100 000 electrons with energy 0.5 MeV are distributed uniformly in the CD. We fit parameters and select models in Eq. (10) by the likelihood

$$\begin{aligned} \log \mathcal{L} &= \log \left\{ \prod_k R^0(t_k; r_{i_k}, \theta_{j_k i_k}) \prod_{i,j} \exp \left[- \int R^0(t; r_i, \theta_{ji}) dt \right] \right\} \\ &= \underbrace{\sum_k \log R^0(t_k; r_{i_k}, \theta_{j_k i_k})}_{\text{time part}} - \underbrace{\sum_{i,j} \int R^0(t; r_i, \theta_{ji}) dt}_{\text{PE part}}, \end{aligned} \quad (11)$$

where i, j and k are indices of the event, SiPM and PE. The ‘‘PE part’’ includes all the events and SiPMs, while the ‘‘time part’’ contains PE times t_k with their corresponding events i_k and SiPMs j_k .

3 Tweedie electronic time-charge likelihood

Tan [31] formulates the PDF of single electron response (SER) charge distribution in a Gaussian $f_N(Q; \mu_Q, \sigma_Q^2)$ and the PE count N_{PE} in Poisson $\pi(\lambda)$ where λ is the expectation. The charge PDF of SiPM or PMT is:

$$p(Q; \lambda, \mu, \sigma^2) = \sum_{N_{\text{PE}}=0}^{\infty} f_N(Q; N_{\text{PE}}\mu_Q, N_{\text{PE}}\sigma_Q^2) p_{\pi}(N_{\text{PE}}; \lambda). \quad (12)$$

Although widely followed, it makes no physical sense for the Gaussian distribution to allow a negative charge. We follow Kalousis et al. [32] to use a Gamma distribution $\Gamma(k, \theta)$ to model the SER charge distribution, where k and θ are the shape and scale parameters. Therefore, the distribution of total charge Q

$$f_{\text{Tw}}(Q; \lambda, k, \theta) = \sum_{N_{\text{PE}}=0}^{\infty} f_{\Gamma}(Q; N_{\text{PE}}k, \theta) p_{\pi}(N_{\text{PE}}; \lambda), \quad (13)$$

follows compound Poisson-Gamma distribution. It is a special case of the Tweedie distribution [33] where the Tweedie index parameter ξ satisfies $1 < \xi < 2$ [34]. Tweedie distribution includes the fluctuation of PE count, thus the infinite N_{PE} summation in Eq. (12) is shifted to standard routines [35,36]. The parameter relationship between Tweedie distribution and its corresponding Poisson and Gamma distribution[37] is:

$$\begin{cases} \lambda = \frac{\mu^{2-\xi}}{\phi(2-\xi)} \\ k = \frac{2-\xi}{\xi-1} \\ \theta = \phi(\xi-1)\mu^{\xi-1}, \end{cases} \quad (14)$$

where μ and ϕ are the mean value and dispersion parameters of Tweedie distribution.

3.1 Parameter calibration

Tweedie distributions is a special case of exponential dispersion models (EDM) [38]. Generalized linear model (GLM) [39,37] is available for Eq. (13) to establish the relationship between the expected PE count λ and charge Q . Specifically, we use the following expression of GLM,

$$\begin{cases} Q \sim \text{Tw}(\mu, \phi, \xi) \\ \mu = b\lambda, \end{cases} \quad (15)$$

with an identity link function $g(\mu) = \mu$. The intercept of linear predictor is zero. λ is predicted by the optical response from Eq. (5) as the input to GLM. According to Eq. (14),

$$\lambda k\theta = \mu \xrightarrow{\mu=b\lambda} b = k\theta = E[Q|N_{\text{PE}} = 1], \quad (16)$$

the slope b is the expected charge of a single PE.

For simplicity, we ignore the variations of the SiPM-tile Tweedie parameters in the Monte Carlo. In the future we shall calibrate the real detector channel-by-channel. Figs. 5a and 5b show the charge distribution of a selected SiPM for 10,000 1 MeV and 3 MeV electrons located at the center of CD, where λ is kept constant. These charges are generated by *electronic simulation* considering dark noise, afterpulse and internal crosstalk [40].

Our electronic simulation includes internal crosstalk, where every PE might induce another PE in the SiPM. It breaks the Poisson assumption in Eq. (13) and necessitates a generalized Poisson [41,42] suggested by Vinogradov [43], with a probability mass function (PMF) of

$$f_{\text{GP}}(x; \theta, \eta) = \frac{\theta(\theta + \eta x)^{x-1} e^{-\theta - \eta x}}{x!}. \quad (17)$$

It is verified to work in V. Chmill [44] and Jack Rolph [45]'s studies.

Although when the crosstalk rate $\eta \rightarrow 0$ Eq. (17) degenerates back to a Poisson, the extended compound distribution is generally not in the Tweedie family any more. Fortunately, when λ is not much larger than 1 and the probability of crosstalk is as low as $\sim 15\%$, the effect is not serious. The Tweedie model of Eq. (13)

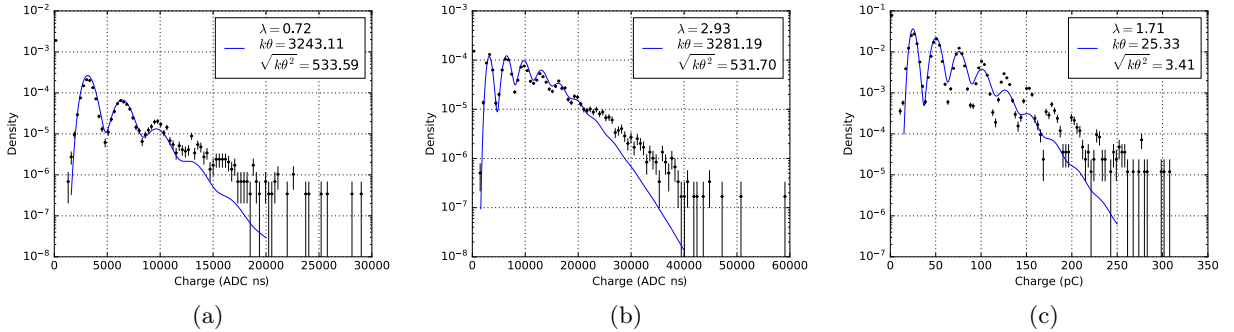


Fig. 5: (a) and (b) are charge distributions of a SiPM tile for 10,000 1 MeV and 3 MeV electrons fixed at center of CD (Monte Carlo simulation). (c) is the charge distribution from one channel output of SiPM tile (experimental data). Solid lines are the regression results of Tweedie GLM, where the parameters of Poisson (λ) and Gamma (k and θ) parts are listed. The units of charge have a conversion factor between ADC ns and pC that do not challenge the validity of the Tweedie model.

is validated against a laboratory test of a SiPM sample in Fig. 5c. The data and model exhibits difference at the higher charge tails of the distribution, similar to the Monte Carlo in Fig. 5b. Momentarily, we regard the convenience of Tweedie GLM to surpass the imperfectness of the Poisson assumption, as will be supported by the reconstruction results in Sec. 4. We shall develop regression with the compound of generalized Poisson and Gamma distribution in our future publications.

3.2 Charge-only reconstruction likelihood

For some small detectors, time readout is usually not important. The expected PE count in the electronic time window $[\underline{T}, \bar{T}]$ is

$$\lambda_{j, [\underline{T}, \bar{T}]}(\vec{r}, E) = v(E) \int_{\underline{T}}^{\bar{T}} R_j^0(t; \vec{r}) dt = v(E) \lambda_{j, [\underline{T}, \bar{T}]}^0(\vec{r}).$$

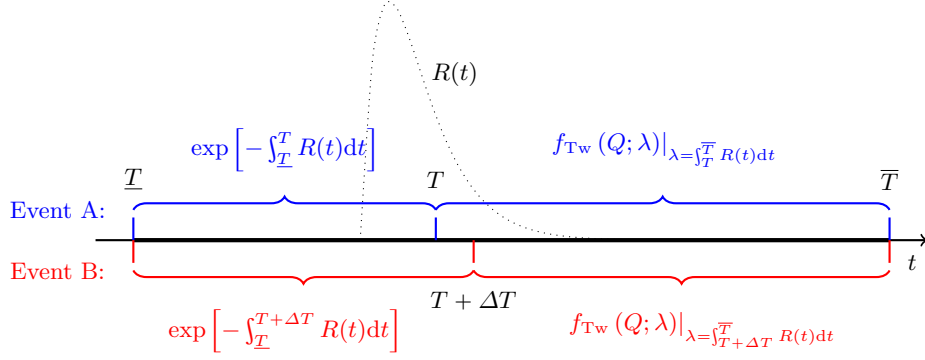


Fig. 6: Diagram of response function $R(t)$ (dotted line), event A (blue) and event B (red) along the time axis. Event A contains Event B due to the one-way dimension of object time t and $\Delta T > 0$. The probabilities of each sub events are listed.

A charge-only reconstruction likelihood is a direct consequence of the Tweedie distribution in Eq. (13) and the optical model in Eq. (2),

$$L(\vec{r}, v_E; \{Q_j\}) = \prod_{j=1}^{N_{\text{SiPM}}} f_{\text{Tw}}(Q_j; bv_E \lambda_{j, [\underline{T}, \bar{T}]}^0(\vec{r}), \phi, \xi), \quad (18)$$

where b , ϕ and ξ are calibrated before event reconstruction. v_E is an alternative notation for $v(E)$ just to remind us that visible energy is the target of the likelihood-based estimation. It is $v(E)$ instead of the kinetic energy E that needs to be treated as a parameter.

The dark hits from SiPM follows a homogeneous Poisson process of intensity $R_D = 46\,086$ Hz in our Monte Carlo. By the superposition property of Poisson process, it is incorporated into the optical model at Eq. (18) by replacing $R_j(\cdot)$ with $R_j(\cdot) + R_D$

$$\begin{aligned} \lambda_{j, [\underline{T}, \bar{T}]}(\vec{r}, E) &= \int_{\underline{T}}^{\bar{T}} [R_j(t; \vec{r}, E) + R_D] dt \\ &= v(E) \lambda_{j, [\underline{T}, \bar{T}]}^0(\vec{r}) + R_D \cdot (\bar{T} - \underline{T}). \end{aligned} \quad (19)$$

3.3 Time-charge reconstruction likelihood

The time-charge reconstruction is challenging to get correct because of the inter-dependence between the two variables. The charge Q affects first hit time T indirectly via the PE counts, not to be confused with the time-walk [46] which is a time error caused by varying amplitude of pulses and a constant threshold. Conversely, an observed T implies the integrated charge is only contributed by the time window of $[\underline{T}, \bar{T}]$. It invalidates all the prevents efforts trying to decouple the time-charge reconstruction likelihood into time and charge parts. Instead, we should start from first principles to derive the joint distribution of T and Q .

For clarity in the following derivation, we write $R(t)$ to mean $R_j(t; \vec{r}, E)$. Consider the following two events. *Event A*: There is no PE or charge in $[\underline{T}, T]$. *Event B*: There is no charge in $[\underline{T}, T + \Delta T]$ ($\Delta T > 0$). Obviously, $B \subset A$. Fig. 6 shows the probabilities of both events. The set difference $A \setminus B$ has a physical meaning that there is no charge in $[\underline{T}, T]$, and there is a PE in $[T, T + \Delta T]$, and the Q is generated by $\int_T^{\bar{T}} R(t)dt$. The difference of their probabilities is

$$\begin{aligned} f_{\text{TQ}}[T, Q; R(t)]\Delta T &= \overbrace{\exp\left[-\int_{\underline{T}}^T R(t)dt\right] f_{\text{Tw}}(Q; \lambda)|_{\lambda=\int_{\underline{T}}^{\bar{T}} R(t)dt}}^{\text{Event A}} \\ &\quad - \underbrace{\exp\left[-\int_{\underline{T}}^{T+\Delta T} R(t)dt\right] f_{\text{Tw}}(Q; \lambda)|_{\lambda=\int_{\underline{T}}^{T+\Delta T} R(t)dt}}_{\text{Event B}}. \end{aligned} \quad (20)$$

Table 1: e^- datasets used for calibration of response and evaluation of reconstruction methodology

Usage	Section	Simulation stage	Configuration
Optical model	2	detector	0.5 MeV e^- uniformly in CD
Electronic model	3	detector + electronic	1 MeV and 3 MeV e^- at the detector center
Evaluation	4	detector + electronic	0.5 ~ 7.5 MeV e^- along the x-axis

When $\Delta T \rightarrow 0$,

$$\begin{aligned}
f_{\text{TQ}}[T, Q; R(t)] &= -\frac{\partial}{\partial T} \left\{ \exp \left[-\int_{\underline{T}}^T R(t) dt \right] f_{\text{TW}}(Q; \lambda) \Big|_{\lambda=\int_{\underline{T}}^T R(t) dt} \right\} \\
&= \exp \left[-\int_{\underline{T}}^T R(t) dt \right] R(T) \left(1 + \frac{\partial}{\partial \lambda} \right) f_{\text{TW}}(Q; \lambda) \Big|_{\lambda=\int_{\underline{T}}^T R(t) dt}.
\end{aligned} \tag{21}$$

Eq. (21) is the joint distribution of charge Q and first hit time T , whose normalization is verified in Appendix A.

When $R(t) \equiv \rho$ is a constant, the time terms of Eq. (21) resembles a random-start waiting time of a paralyzable deadtime [47] with length $T - \underline{T}$,

$$g(t) = \rho \exp[-\rho(T - \underline{T})]. \tag{22}$$

At TAO, any PE is only registered in a trigger-initiated data-taking window. That is different from a nuclear counting circuit where signals are continuously recorded. Despite this, they do share the same logic that a signal cannot be registered if there is another one in the preceding deadtime interval. Consequently, TAO electronics appears to have a varied deadtime $T - \underline{T}$ according to the location of the first PE in the time window.

Expanding $R(t)$ back to $R_j(t; \vec{r}, E)$, the reconstruction likelihood is

$$\begin{aligned}
L(\vec{r}, v_E, t_0; \{(T_j, Q_j)\}) &= \prod_{\substack{Q_j > 0 \\ \text{hit}}} f_{\text{TQ}}[T_j, Q_j; v_E R_j^0(t - t_0; \vec{r})] \times \prod_{\substack{Q_j = 0 \\ \text{nonhit}}} p_\pi(0; v_E \lambda_{j, [\underline{T}-t_0, \bar{T}-t_0]}^0(\vec{r})) \\
&= \prod_{Q_j > 0} \left\{ \exp \left[-v_E \lambda_{j, [\underline{T}-t_0, T_j-t_0]}^0(\vec{r}) \right] v_E R_j^0(T_j - t_0; \vec{r}) \cdot \left(1 + \frac{\partial}{\partial \lambda} \right) f_{\text{TW}}(Q_j; \lambda) \Big|_{\lambda=v_E \lambda_{j, [T_j-t_0, \bar{T}-t_0]}^0(\vec{r})} \right\} \\
&\quad \times \prod_{Q_j = 0} \exp \left[-v_E \lambda_{j, [\underline{T}-t_0, \bar{T}-t_0]}^0(\vec{r}) \right],
\end{aligned} \tag{23}$$

where t_0 is the event time and j is the index of SiPM. Inclusion of dark hits is straightforward by substituting $R_j(\cdot)$ with $R_j(\cdot) + R_D$ as Eq. (19).

4 Numerical experiment

Calibration runs with radioisotopes [1] will be the benchmark for event reconstruction. Before such data are available, we deploy Monte Carlo simulation to fit the coefficients of response function and evaluate the reconstruction.

Electrons with fixed energies and vertices along the x -axis are simulated. The simulation is carried out in two stages. *Detector* and *electronic simulation* cover the processes before and after a photon hits a SiPM. PEs, the information carriers for event reconstruction, are smeared in both number and times in *electronic simulation*. Detector simulation characterizes the optical model while the complete simulation with two stages is for accessing the reconstruction performance. Table 1 summarizes the simulated datasets.

We access two variants of reconstruction likelihood functions in Eqs. (18) and (23).

4.1 With charge Q

The first column of Fig. 7 shows the reconstruction by charge using Eq. (18). Fig. 7a gives the bias of reconstructed vertices along the x -axis. The maximum bias in the fiducial volume (FV) is about 5.0 mm, which occurs around radius of 400 mm. Vertices near the boundary of CD won't be mis-reconstructed into the FV. The vertex bias is caused by the approximation of intensity function Eq. (5). For vertex resolution shown in Fig. 7c, we find it decrease with energy at < 3 MeV but increase at > 3 MeV. At low energy, an electron deposits its energy within several millimeters. The vertex resolution is determined by sheer quantity of photons. At high energy, an electron travels centimeters long that is comparable to the vertex resolution. The resolution gets worse with longer tracks.

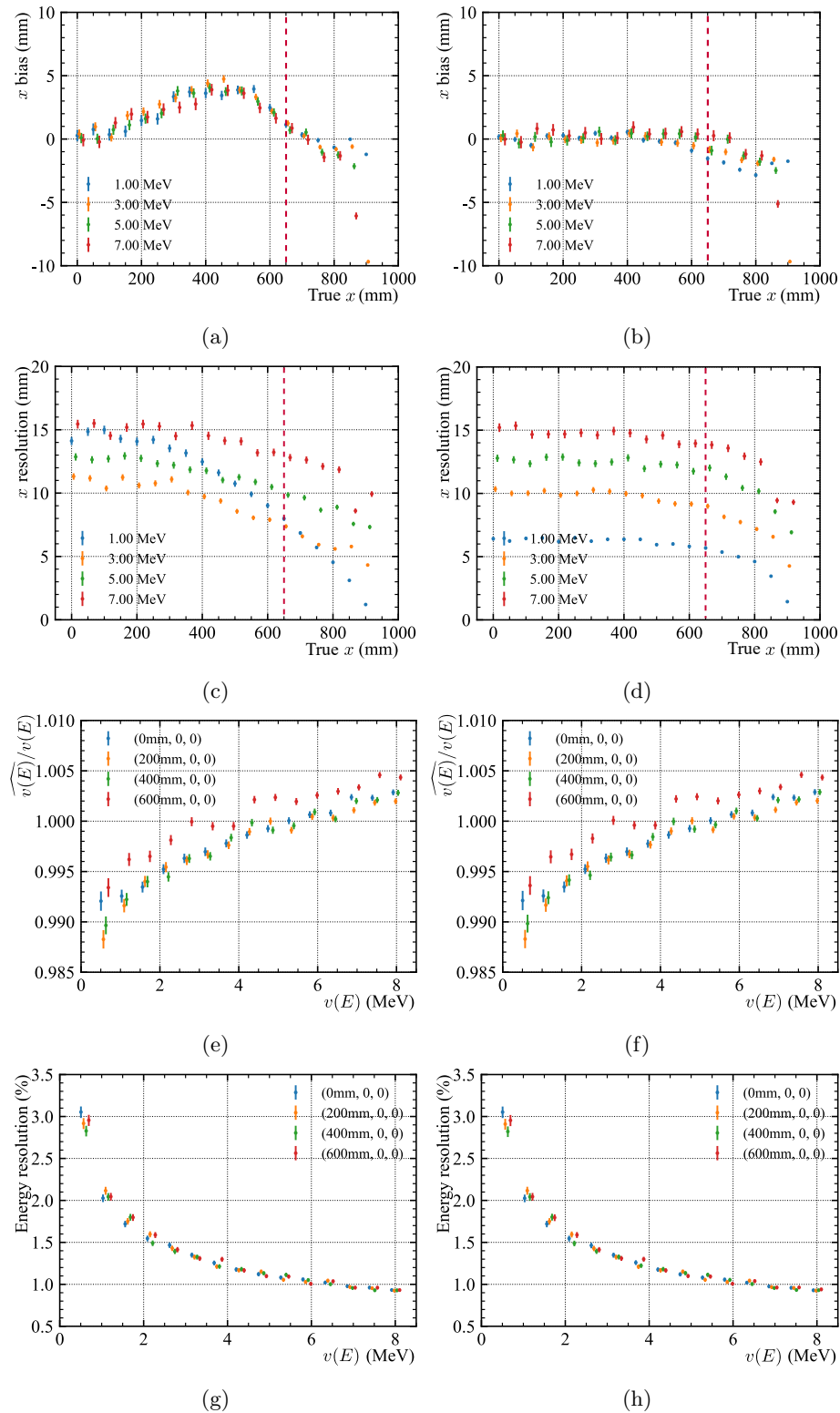


Fig. 7: The reconstruction results of vertex position (x coordinates) and energy using charge (first column) and first hit time(second column). (a), (b), (c) and (d) show the reconstruction bias and resolution (standard deviation) of x coordinates, with vertical dashed lines marking the boundary of fiducial volume; (e), (f), (g), (h) show the reconstruction bias and resolution (relative standard deviation) of visible energy. The data points are shifted horizontally for visibility.

We define the visible energy $v(E)$ of an event as a linear scale from the expected number of PEs $\langle N_{\text{PE}}(E) \rangle = \langle \sum_{j=1}^{N_{\text{SiPM}}} p_j N_{\text{PE},j}(E) \rangle$ if it were at the detector center, with the conversion factor that makes an electron with

0.5 MeV kinetic energy the same visible energy of 0.5 MeV,

$$v(E) = \frac{\langle \sum_{j=1}^{N_{\text{SiPM}}} p_j N_{\text{PE},j}(E) \rangle}{\langle \sum_{j=1}^{N_{\text{SiPM}}} p_j N_{\text{PE},j}(0.5 \text{ MeV}) \rangle} 0.5 \text{ MeV}, \quad (24)$$

while p_j indicates the differences of photon detection efficiency (PDE) among SiPM tiles. In the simulation these PDEs are the same. We ignore the p_j in (24) and use the simplified form,

$$v(E) = \frac{\langle \sum_{j=1}^{N_{\text{SiPM}}} N_{\text{PE},j}(E) \rangle}{\langle \sum_{j=1}^{N_{\text{SiPM}}} N_{\text{PE},j}(0.5 \text{ MeV}) \rangle} 0.5 \text{ MeV} = \frac{\langle N_{\text{PE}}^0(E) \rangle}{\langle N_{\text{PE}}^0(0.5 \text{ MeV}) \rangle} 0.5 \text{ MeV}. \quad (25)$$

Fig. 7e shows the ratio of reconstructed energy $\widehat{v(E)}$ versus visible energy $v(E)$, which is caused by the deviation from linearity between PE count and output charge on SiPMs, known as *electronics non-linearity*. In order to quantify the effect, we do a linear fit without intercept on to predict charge Q from the PE count N_{PE} . N_{PE} contains physical PEs that is proportional to visible energy $v(E)$ and dark counts N_{dn} . The relative residual $(\hat{Q} - Q)/Q$ in Fig. 8 matches with Fig. 7e in both shape and magnitude. Contribution from white noise

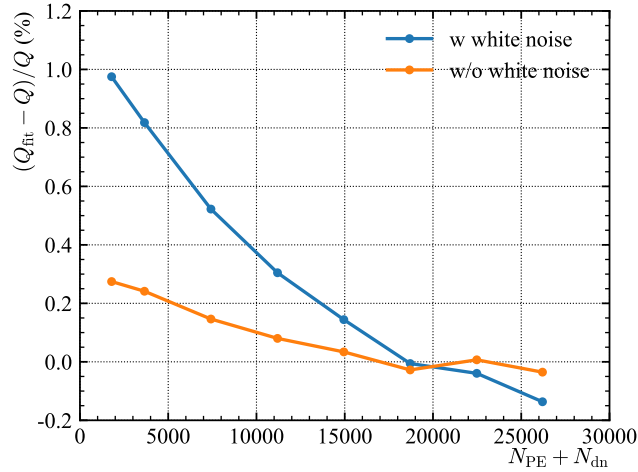


Fig. 8: The relative residual of $Q \sim N_{\text{PE}}$ indicates the electronics non-linearity. The test data are electrons located at center of CD.

dominates the electronics non-linearity.

Fig. 7g shows the resolution of energy reconstruction to be slightly over 2% at 1 MeV. We shall discuss it more around Eq. (26) in the next section.

4.2 With charge Q and accurate first hit time T

It is well known that time is not useful in meter-scaled detectors [14]. But TAO is so special that we set out to explore the value of time information. In this section, the first hit times are extracted from the detector simulation without imposing electronic smears to evaluate its best possible contribution.

The right column of Fig. 7 shows the reconstruction using charge and first hit time. The bias of vertex reconstruction shown in Fig. 7b increases with radius. In the FV $r < 650$ mm, the maximum bias is 2.0 mm, substantially less than that using only charge in Fig. 7a. The vertex resolution in Fig. 7d is better than that using charge only especially for low energy (~ 1 MeV). In the FV, it shows a new flat trend with time, because the accuracy of times only degrades slightly due to dispersion when a source moves away from SiPMs, much less sensitive than that of charges. Our results show that time plays an important role in reducing the bias and resolution of vertex reconstruction.

The bias and resolution in Fig. 7f and Fig. 7h are essentially the same as the results with charge alone, indicating that the energy reconstruction is dominated by the charge. The data points of energy resolution in Figs. 7g and 7h are fitted with Eq. (26)[48]:

$$\frac{\sigma}{v(E)} = \sqrt{\left(\frac{a}{\sqrt{v(E)}}\right)^2 + b^2 + \left(\frac{c}{v(E)}\right)^2}, \quad (26)$$

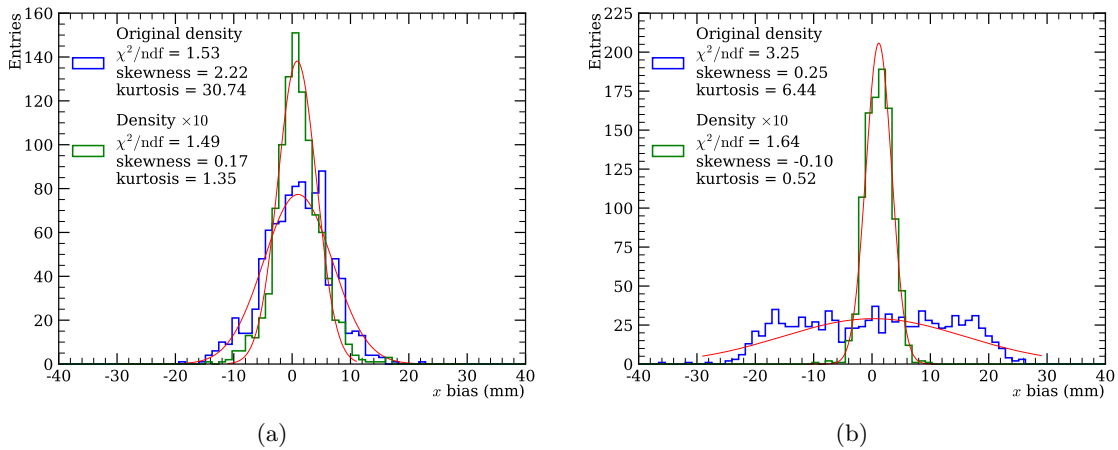


Fig. 9: Distribution of reconstructed x position for 0.5 MeV (a) and 5.0 MeV (b) electrons. Green and blue lines represents the two different GdLS densities. Red lines are fitted with Gaussian. At higher energy, the shape of distribution is affected by the electron tracks, breaking the point-like assumption.

where a denotes the Poisson statistical contribution from the PE count; b is related to energy non-linearity and non-uniformity, including quenching effect, Cherenkov radiation and electronics non-linearity; c reflects the influence of dark noise. The best-fit results of a , b and c are 2.002 %, 0.656 % and 8.31×10^{-5} %, respectively. The fitted energy resolution at 1 MeV kinetic energy is 2.07 %.

The electron track effect is evident when we look closer into the distribution of reconstructed vertices in Fig. 9. The flat-shaped vertex distribution of electrons at 5.0 MeV deviates from Gaussian. In our point-model, a reconstructed vertex is the barycenter of the energy deposition along the track, which is shifted from the starting point in the direction of the e^- momentum. The projection of isotropic shifts onto the x -axis results in the flat distribution. To verify our speculation, we artificially enlarge the GdLS density 10 times so that the mean free path of 5.0 MeV e^- is less than 1 mm. The resulting distribution of reconstructed x shown in green of Fig. 9 returns to Gaussian as expected. For better modeling, we should no longer treat e^- of several MeV as point sources. With the introduction of tracks in our future work, the reconstructed vertex should be the starting point of the track rather than the energy-deposition barycenter.

Our tests support the feasibility of reconstruction using first hit time and charge according to a pure probabilistic model introduced in Sec. 2 and Sec. 3.2.

4.3 With charge Q and smeared first hit time T_s

In reality, the first hit time T is smeared by intrinsic transit time spread (TTS), but for SiPM TTS is at the level of 100 ps. Discrete sampling of analog-digital converter (ADC) and time walk effects impose larger time uncertainty than TTS at TAO, though they could in principle be mitigated by clever firmware design. In this section, we consider two extreme cases of time blurring, 0.1 ns for TTS alone and 8 ns for the sampling interval of ADC.

Without loss of generality, we add a Gaussian smear $\Delta T \sim N(0, \sigma^2)$ to each PE in a SiPM channel, where the first PE might be overtaken by the second one after the smearing. The updated *smeared first hit time* T_{sj} substitutes T_j in Eq. (23). Meanwhile, the response function Eq. (10) is convoluted with the same Gaussian kernel. Fig. 10 gives a series of position resolution plots for σ running from 0.1 to 8.0 ns. Only position resolution of ~ 1 MeV e^- changes significantly because that of higher energy e^- is dominated by track effect (Fig. 9). As σ becomes larger, the resolution of ~ 1 MeV transits from time to charge dominance.

Energy reconstruction with Q and T_s are consistent with those in Fig. 7.

Because of time in likelihood function Eq. (23), the algorithm can also give the reconstructed event time t_0 . Figs. 11a and 11b are the bias and resolution of time reconstruction respectively, which shows the same trend over energy, as the reconstruction results of vertex resolution using only charge. The time bias is the difference between reconstructed event time t_0 and the real event time (default zero) in detector simulation. In reality t_0 is affected by trigger time and time delay in cable [18], thus the result of time bias is provided as a reference. The time resolution without considering TTS is less than 0.02 ns.

5 Discussion

Our model is applicable to other neutrino detectors. There are several points to be improved.

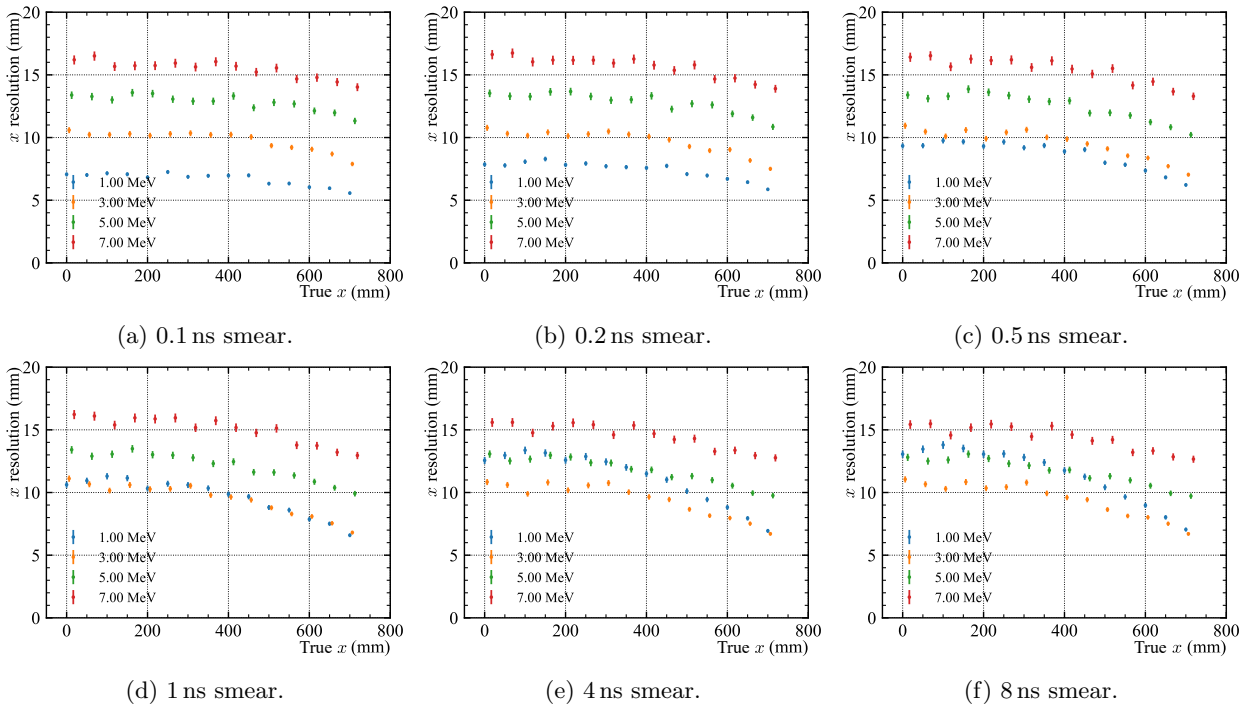


Fig. 10: The reconstruction results of position resolution with charge Q and smeared first time T_s . (a)–(f) show the changes of vertex resolution for blurring $\sigma = 0.1$ to 8.0 ns. 1 MeV and lower energy events are affected the most by time accuracy while 5 MeV and higher energy events are dominated by their track effect.

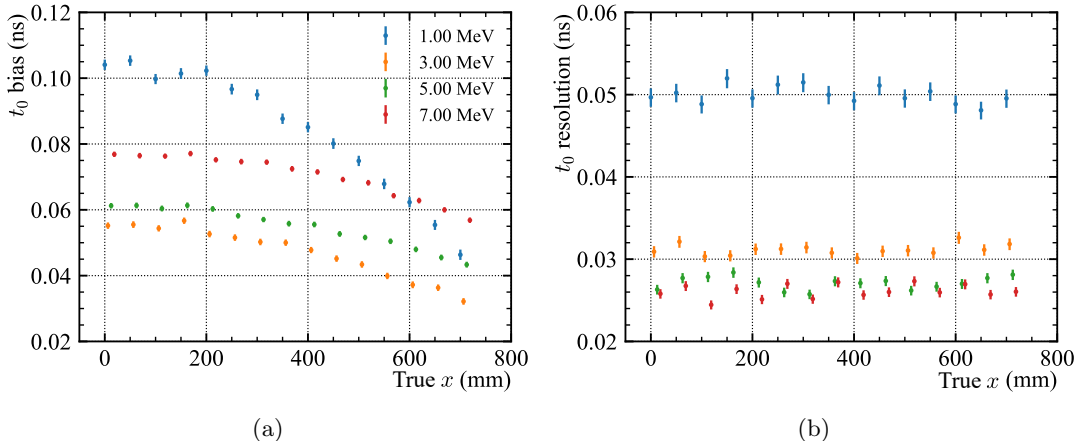


Fig. 11: Bias (a) and resolution (b) of the reconstructed event time t_0 with 1.0σ smeared first hit time.

5.1 Related work

Z. Li et al. [18] use the charge to estimate the PE count roughly, according to average charge of one PE on PMT. The construction of nPE map in G. Huang's work [19] shares the similar shortcoming. Due to the fluctuation of charge for one PE, it is impossible to get an accurate PE count considering only one charge value. Although waveform analysis [49] is helpful to determine the PE count and timing, it cannot be applied to time and charge readouts. Tweedie distribution takes into account the fluctuations of PE count and charge, thus inherently solving the above problem. Nonetheless, the dependency between first hit time T and PE count N is also important. It is the foundation to understand the time-charge dependency and reconstruct with T and N . The joint distribution $f_{TN}[T, N; R(t)]$ can be derived with a similar method discussed in Sec. 3.3. Or just simply replace the Tweedie distribution $f_{Tw}(Q; \lambda)$ in Eq. (21) with the Poisson probability of N

$$p_{\pi}(N; \lambda) = \exp(-\lambda)\lambda^N/N!, \quad (27)$$

and then derive the joint distribution

$$f_{TN}[T, N; R(t)] = \frac{\exp(-\lambda_{[T, \bar{T}]})R(T)\lambda_{[T, \bar{T}]}^{N-1}}{(N-1)!}. \quad (28)$$

The normalization of Eq. (28) can also be verified. Eq. (28) is so-called first photoelectron timing technique [18], which was also derived by G. Ranucci [13], later by C. Galbiati and K. McCarty [14]. The form of reconstruction likelihood is similar to Eq. (23):

$$\begin{aligned}
L(\vec{r}, v_E, t_0; \{(T_j, N_j)\}) &= \prod_{\substack{N_j > 0 \\ \text{hit}}} f_{\text{TN}} [T_j, N_j; v_E R_j^0(t - t_0; \vec{r})] \times \prod_{\substack{N_j = 0 \\ \text{nonhit}}} p_{\pi} \left(0; v_E \lambda_{j, [\underline{T}-t_0, \bar{T}-t_0]}^0(\vec{r}) \right) \\
&= \prod_{N_j > 0} \left\{ \frac{1}{(N_j - 1)!} \exp \left[-v_E \lambda_{j, [\underline{T}-t_0, \bar{T}-t_0]}^0(\vec{r}) \right] v_E R_j^0(T_j - t_0; \vec{r}) \left[v_E \lambda_{j, [T_j - t_0, \bar{T}-t_0]}^0(\vec{r}) \right]^{N_j - 1} \right\} \\
&\quad \times \prod_{N_j = 0} \exp \left[-v_E \lambda_{j, [\underline{T}-t_0, \bar{T}-t_0]}^0(\vec{r}) \right].
\end{aligned} \tag{29}$$

5.2 Application of Tweedie GLM on PMT

Compared to SiPM's charge spectrum, that of PMT has greater variance in Gamma part of Tweedie distribution, and it can also be fitted with Tweedie GLM. Fig. 12 shows a charge spectrum of PMT extracted from Fig. 1 in Kalousis's report [50] and the fitting result using Tweedie distribution. The charges around the pedestal are neglected in the fitting and considered as zero. It indicates that Tweedie GLM is not only suitable for charge distribution of SiPM with low crosstalk, but also for PMT spectrum modeled by Kalousis [50] and Anthony et al. [51].

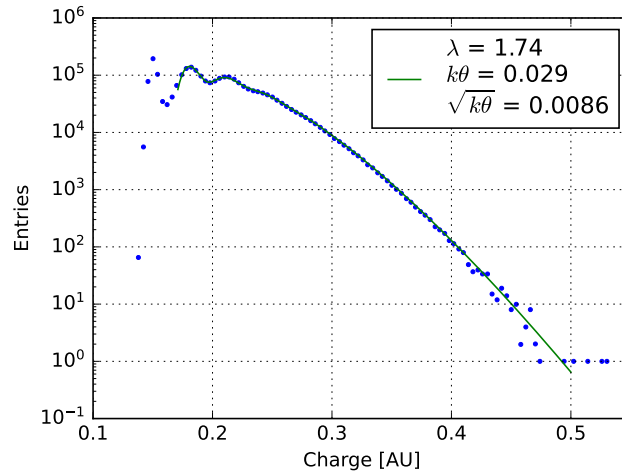


Fig. 12: Charge distribution of PMT (blue point) and fitting result using Tweedie distribution (solid line). The first peak is the pedestal and the second one is the single photoelectron peak. The proportion of charge near the pedestal is about 0.175, which is consistent with the fitting results $\exp(-\lambda) \approx 0.176$. The charge spectrum is extracted from Fig. 1 in Kalousis's report [50].

5.3 The importance of T on other detectors

Figs. 7e, 7f, 7g and 7h indicates that the time inputs have negligible improvement on energy reconstruction for TAO. Due to high photo-coverage ($\sim 94\%$) and photon detection efficiency ($> 50\%$) of TAO detector, charge-only point-like reconstruction is comparable to the T-Q combined one. Both of them introduce little non-uniformity.

Nevertheless, the time inputs and the T-Q combined likelihood (Eq. 23) have significant potential for vertex and energy reconstruction at larger LS detectors. Position reconstruction is more sensitive to time than charge, and it impacts on energy resolution via non-uniformity.

5.4 Track effect in reconstruction

In Sec. 4, we achieve a vertex position resolution better than 20 mm for point-like events, which is much greater than the requirement in TAO CDR [12]. We find the non-Gaussian distribution of position reconstruction

in Fig 9a and worsening resolution of vertex position with e^- energy in Figs. 7c and 7d. Both imply that traditional assumption of point-like source is not appropriate for MeV e^- .

The effect is more manifested with e^+ and γ as their energy deposits are multi-sited. It demands to extend the point-like model to a track-like one for meticulous reconstruction. The prerequisite is precise time measurement in electronics, which is crucial to ameliorate position resolution (Fig. 10).

The dynamics of track-like events are governed by the physics laws of positron annihilation, Compton scattering and photoemission of electrons. Embedding them into reconstruction will give powerful constraints on the allowed parameter space. It will lead to rigorous estimates of vertex and momentum of an incident particle. Additionally, it is helpful to moderate the impact of energy leakage on e^+ and γ energy resolution.

Future track-like reconstruction depends strongly on the precise time measurement. It is important to deploy ADC with higher time precision and develop electronics firmware with the advanced time-over-threshold [52, 53] to improve time resolution.

5.5 Calibration of the optical detector model

Our model is based on Monte Carlo simulation of 0.5 MeV e^- to give a perfect point-source response. However, the most common radioactive source deployed in detector calibration is the γ source, such as ^{137}Cs and ^{60}Co . The γ deposits energy at the scale of 10 cm and cannot be used directly to construct $R^0(\cdot)$ in Eq. 10. We are developing a robust algorithm to extract point-source response from γ calibrations by properly modeling the track-effects of γ .

5.6 External crosstalk

External crosstalk or *optical crosstalk* is the processes involving photon emission of a SiPM that registers PEs on the surrounding SiPMs. The mechanism can be compared to PMT flashers. External crosstalk is suitable to be included in the optical detector model and should not be included in the charge model, because it involves multiple SiPMs and resembles diffuse reflections of photons. We shall model the external crosstalk after the *in situ* characterization of external crosstalk of SiPM is obtained during TAO commissioning.

6 Conclusion

From first principles, a pure probabilistic methodology is proposed to simultaneously reconstruct vertex, energy and time for point-like events in TAO CD and shown to meet the requirement and perform well. In fiducial volume of TAO detector and energy range of reactor neutrinos, after considering the dark noise and direct crosstalk of SiPMs, for 1 MeV e^- , position resolution better than 20 mm energy resolution of 2% is achieved. It does not impose extra non-linearity from reconstruction, controlling it within 0.4%. Owing to high photon-detection efficiency and precise time measurement, the track effect for MeV e^- is evident. This methodology sufficiently utilizes first hit time and charge in reconstruction, which can be used not only for SiPM in TAO detector, but also for other experiments with first hit time and charge readouts, such as 3-inch PMT in JUNO [54] and QBEE electronics in Super-Kamiokande [55].

Acknowledgments

We are grateful to Yuyi Wang for proofreading the manuscript. We also thank Yiyang Wu, Jun Weng and Aiqiang Zhang for discussions of reconstruction algorithms and development of SiPM/PMT charge model using Poisson and Gamma distributions. We appreciate the help of JUNO collaboration which keeps our research on track.

The idea of first-principle time-charge likelihood originates from the draft *va3* fitter at KamLAND [56]. It grew out of the reconstruction parameter tuning guided by Prof. Itaru Shimizu, and received scrutinization and encouragement from Prof. Jason Detwiler. The corresponding author would like to sincerely appreciate the KamLAND collaboration for education and inspirations on event reconstruction and neutrino physics. This work is supported by the National Natural Science Foundation of China (No.123B2078).

References

1. Hangkun Xu et al. Calibration strategy of the JUNO-TAO experiment. *The European Physical Journal C*, 82(12):1112, December 2022.
2. Patrick Huber. Determination of antineutrino spectra from nuclear reactors. *Phys. Rev. C*, 84:024617, Aug 2011.

3. Th. A. Mueller, D. Lhuillier, M. Fallot, A. Letourneau, S. Cormon, M. Fechner, L. Giot, T. Lasserre, J. Martino, G. Mention, A. Porta, and F. Yermia. Improved predictions of reactor antineutrino spectra. *Phys. Rev. C*, 83:054615, May 2011.
4. F. P. An et al. Measurement of the reactor antineutrino flux and spectrum at Daya Bay. *Phys. Rev. Lett.*, 116:061801, Feb 2016.
5. H. de Kerret et al. Double Chooz θ_{13} measurement via total neutron capture detection. *Nature Phys.*, 16(5):558–564, 2020.
6. G. Bak et al. Measurement of reactor antineutrino oscillation amplitude and frequency at RENO. *Phys. Rev. Lett.*, 121:201801, Nov 2018.
7. Y. J. Ko et al. Sterile neutrino search at the NEOS experiment. *Phys. Rev. Lett.*, 118:121802, Mar 2017.
8. H. Almazán et al. STEREO neutrino spectrum of ^{235}U fission rejects sterile neutrino hypothesis. *Nature*, 613(7943):257–261, 2023.
9. D. Adey et al. Extraction of the ^{235}U and ^{239}Pu antineutrino spectra at Daya Bay. *Phys. Rev. Lett.*, 123:111801, Sep 2019.
10. Angel Abusleme et al. JUNO physics and detector. *Prog. Part. Nucl. Phys.*, 123:103927, 2022.
11. A. A. Sonzogni, M. Nino, and E. A. McCutchan. Revealing fine structure in the antineutrino spectra from a nuclear reactor. *Phys. Rev. C*, 98:014323, Jul 2018.
12. Angel Abusleme et al. TAO Conceptual Design Report: A Precision Measurement of the Reactor Antineutrino Spectrum with Sub-percent Energy Resolution. 5 2020.
13. Gioacchino Ranucci. An analytical approach to the evaluation of the pulse shape discrimination properties of scintillators. *Nuclear Instruments and Methods in Physics Research Section A: Accelerators, Spectrometers, Detectors and Associated Equipment*, 354(2):389–399, 1995.
14. C. Galbiati and K. McCarty. Time and space reconstruction in optical, non-imaging, scintillator-based particle detectors. *Nuclear Instruments and Methods in Physics Research Section A: Accelerators, Spectrometers, Detectors and Associated Equipment*, 568(2):700–709, 2006.
15. Mikhail Batygov. *Combined Study of Reactor and Terrestrial Antineutrinos with KamLAND*. PhD thesis, University of Tennessee, Knoxville, 2006.
16. G. Bellini et al. Final results of Borexino Phase-I on low-energy solar neutrino spectroscopy. *Phys. Rev. D*, 89:112007, Jun 2014.
17. M Jiang et al. Atmospheric neutrino oscillation analysis with improved event reconstruction in Super-Kamiokande IV. *Progress of Theoretical and Experimental Physics*, 2019(5):053F01, 05 2019.
18. Zi-Yuan Li et al. Event vertex and time reconstruction in large-volume liquid scintillator detectors. *Nuclear Science and Techniques*, 32:49, 2021.
19. Gui-Hong Huang et al. Data-driven simultaneous vertex and energy reconstruction for large liquid scintillator detectors. *Nuclear Science and Techniques*, 34, 2023.
20. Zhen Qian et al. Vertex and energy reconstruction in jun0 with machine learning methods. *Nuclear Instruments and Methods in Physics Research Section A: Accelerators, Spectrometers, Detectors and Associated Equipment*, 1010:165527, 2021.
21. Arsenii Gavrikov, Yury Malyshkin, and Fedor Ratnikov. Energy reconstruction for large liquid scintillator detectors with machine learning techniques: aggregated features approach. *Eur. Phys. J. C*, 82(11):1021, 2022.
22. Wei Dou et al. Reconstruction of point events in liquid-scintillator detectors subjected to total reflection. 2022.
23. S. Donati, E. Gatti, and V. Svelto. The statistical behavior of the scintillation detector: Theories and experiments. volume 26 of *Advances in Electronics and Electron Physics*, pages 251–307. Academic Press, 1969.
24. D. Adey et al. A high precision calibration of the nonlinear energy response at daya bay. *Nuclear Instruments and Methods in Physics Research Section A: Accelerators, Spectrometers, Detectors and Associated Equipment*, 940:230–242, 2019.
25. F. P. An et al. Spectral measurement of electron antineutrino oscillation amplitude and frequency at daya bay. *Phys. Rev. Lett.*, 112:061801, Feb 2014.
26. J. H. Choi et al. Observation of energy and baseline dependent reactor antineutrino disappearance in the reno experiment. *Phys. Rev. Lett.*, 116:211801, May 2016.
27. Kuo Niu and Chao Tian. Zernike polynomials and their applications. *Journal of Optics*, 24(12):123001, nov 2022.
28. George B. Arfken, Hans J. Weber, and Frank E. Harris. Chapter 15 - legendre functions. In George B. Arfken, Hans J. Weber, and Frank E. Harris, editors, *Mathematical Methods for Physicists (Seventh Edition)*, pages 715–772. Academic Press, Boston, seventh edition edition, 2013.
29. David Jenkins. *Radiation Detection for Nuclear Physics*. 2053-2563. IOP Publishing, 2020.
30. J. Allison et al. Recent developments in Geant4. *Nuclear Instruments and Methods in Physics Research Section A: Accelerators, Spectrometers, Detectors and Associated Equipment*, 835:186–225, November 2016.
31. Harry H. Tan. A statistical model of the photomultiplier gain process with applications to optical pulse detection, 1982.
32. L.N. Kalousis et al. A fast numerical method for photomultiplier tube calibration. *Journal of Instrumentation*, 15(03):P03023, mar 2020.
33. Maurice CK Tweedie et al. An index which distinguishes between some important exponential families. In *Statistics: Applications and new directions: Proc. Indian statistical institute golden jubilee International conference*, volume 579, pages 579–604, 1984.
34. G. K. Smyth. Regression modelling of quantity data with exact zeroes. In *Proceedings of the Second Australia-Japan Workshop on Stochastic Models in Engineering, Technology and Management*, pages 572–580. Technology Management Centre, University of Queensland, 1996.
35. Peter K. Dunn and Gordon K. Smyth. Series evaluation of Tweedie exponential dispersion model densities. *Stat Comput*, 15(4):267–280, October 2005.

36. Peter K. Dunn and Gordon K. Smyth. Evaluation of Tweedie exponential dispersion model densities by Fourier inversion. *Stat Comput*, 18(1):73–86, March 2008.
37. Peter K. Dunn and Gordon K. Smyth. *Generalized Linear Models With Examples in R*. Springer Texts in Statistics. Springer New York, New York, NY, 2018.
38. B Jørgensen. Exponential dispersion models (with discussion). *Journal of the Royal Statistical Society B*, 49:127–162, 1987.
39. P. McCullagh. *Generalized Linear Models*. Chapman and Hall/CRC, Boca Raton, 2nd edition edition, August 1989.
40. Fabio Acerbi and Stefan Gundacker. Understanding and simulating SiPMs. *Nuclear Instruments and Methods in Physics Research Section A: Accelerators, Spectrometers, Detectors and Associated Equipment*, 926:16–35, 2019. Silicon Photomultipliers: Technology, Characterisation and Applications.
41. P.C. Consul and Felix Famoye. Generalized poisson regression model. *Communications in Statistics - Theory and Methods*, 21(1):89–109, 1992.
42. S. Vinogradov. Analytical models of probability distribution and excess noise factor of solid state photomultiplier signals with crosstalk. *Nuclear Instruments and Methods in Physics Research Section A: Accelerators, Spectrometers, Detectors and Associated Equipment*, 695:247–251, 2012. New Developments in Photodetection NDIP11.
43. S. Vinogradov. Analytical models of probability distribution and excess noise factor of solid state photomultiplier signals with crosstalk. *Nuclear Instruments and Methods in Physics Research Section A: Accelerators, Spectrometers, Detectors and Associated Equipment*, 695:247–251, December 2012.
44. V. Chmill et al. On the characterisation of sipms from pulse-height spectra. *Nuclear Instruments and Methods in Physics Research Section A: Accelerators, Spectrometers, Detectors and Associated Equipment*, 854:70–81, 2017.
45. Jack Rolph et al. Peakotron: A python module for fitting charge spectra of silicon photomultipliers. *Nuclear Instruments and Methods in Physics Research Section A: Accelerators, Spectrometers, Detectors and Associated Equipment*, 1056:168544, 2023.
46. Sami Kurtti and Juha T. Kostamovaara. Pulse width time walk compensation method for a pulsed time-of-flight laser rangefinder. *2009 IEEE Instrumentation and Measurement Technology Conference*, pages 1059–1062, 2009.
47. J. W. Müller, V. E. Lewis, D. Smith, J. G. V. Taylor, and G. Winkler. 2. the poisson process. *Reports of the International Commission on Radiation Units and Measurements*, os-27(1):3–11, 1994.
48. Angel Abusleme et al. Prediction of Energy Resolution in the JUNO Experiment. working paper or preprint, June 2024.
49. D.C. Xu et al. Towards the ultimate pmt waveform analysis for neutrino and dark matter experiments. *Journal of Instrumentation*, 17(06):P06040, jun 2022.
50. Leonidas N. Kalousis. An analytical model for photomultiplier tube calibration. *Nuclear Instruments and Methods in Physics Research Section A: Accelerators, Spectrometers, Detectors and Associated Equipment*, 1058:168943, 2024.
51. M. Anthony et al. Characterization of photomultiplier tubes with a realistic model through gpu-boosted simulation. *Journal of Instrumentation*, 13(02):T02011, feb 2018.
52. R. Ota, K. Nakajima, I. Ogawa, and Y. Tamagawa. Dual time-over-threshold: estimation of decay time and pulse height for scintillation detectors. *J. Inst.*, 14(11):P11012, November 2019.
53. H. B. Wang, J. D. Liu, H. J. Zhang, H. Liang, and B. J. Ye. Multiple time-over-threshold readout electronics for fast timing and energy resolving in a SiPM-based positron annihilation lifetime spectrometer. *J. Inst.*, 15(11):P11006, November 2020.
54. S. Conforti et al. Catiroc: an integrated chip for neutrino experiments using photomultiplier tubes. *Journal of Instrumentation*, 16(05):P05010, may 2021.
55. S. Yamada et al. Commissioning of the new electronics and online system for the super-kamiokande experiment. *IEEE Transactions on Nuclear Science*, 57(2):428–432, 2010.
56. Benda Xu. *Observation of Geoneutrinos at KamLAND during Reactor Shutdown*. PhD thesis, Tohoku University, Sendai, Japan, 2014.

A The normalization of f_{TQ}

To verify the normalization of Eq. (21), first integrate T :

$$\begin{aligned}
& \int_{\underline{T}}^{\bar{T}} f_{TQ} [T, Q; R(t)] dT \\
&= - \int_{\lambda_{[\underline{T}, \bar{T}]}}^0 \exp [-(\lambda_{[\underline{T}, \bar{T}]} - \lambda)] \left(1 + \frac{\partial}{\partial \lambda}\right) f_{Tw} (Q; \lambda) d\lambda \\
&= - \int_{\lambda_{[\underline{T}, \bar{T}]}}^0 \frac{\partial}{\partial \lambda} \left\{ \exp [-(\lambda_{[\underline{T}, \bar{T}]} - \lambda)] f_{Tw} (Q; \lambda) \right\} d\lambda \\
&= - \exp [-(\lambda_{[\underline{T}, \bar{T}]} - \lambda)] f_{Tw} (Q; \lambda) \Big|_{\lambda_{[\underline{T}, \bar{T}]}}^0 \\
&= f_{Tw}(Q; \lambda_{[\underline{T}, \bar{T}]}) ,
\end{aligned} \tag{30}$$

Eq. (30) is the Tweedie PDF in 3.2. The first line of Eq. (30) uses

$$d\lambda = -R(T)dT. \tag{31}$$

Then integrate Q , obviously

$$\int f_{Tw}(Q; \lambda_{[\underline{T}, \bar{T}]}) dQ = 1. \tag{32}$$

Of course, we can first integrate Q , but notice if Q is zero:

$$f_{Tw}(Q = 0; \lambda_{[\underline{T}, \bar{T}]}) = \exp(-\lambda_{[\underline{T}, \bar{T}]}) , \tag{33}$$

$$\begin{aligned}
f_T [T; Q \neq 0, R(t)] &= \int f_{TQ} [T, Q; Q \neq 0, R(t)] dQ \\
&= \frac{1}{1 - \exp(-\lambda_{[\underline{T}, \bar{T}]})} \left\{ \int \exp \left[- \int_{\underline{T}}^T R(t) dt \right] R(T) \times \left(1 + \frac{\partial}{\partial \lambda}\right) f_{Tw} (Q; \lambda) \Big|_{\lambda = \int_{\underline{T}}^T R(t) dt} dQ \right\} \\
&= \frac{\exp \left[- \int_{\underline{T}}^T R(t) dt \right] R(T)}{1 - \exp(-\lambda_{[\underline{T}, \bar{T}]})} .
\end{aligned} \tag{34}$$

Eq. (34) is the distribution of first hit time T . Then integrate T ,

$$\int_{\underline{T}}^{\bar{T}} f_T [T; Q \neq 0, R(t)] dT = \frac{- \int_{\lambda_{[\underline{T}, \bar{T}]}}^0 \exp [-(\lambda_{[\underline{T}, \bar{T}]} - \lambda)] d\lambda}{1 - \exp(-\lambda_{[\underline{T}, \bar{T}]})} = 1. \tag{35}$$

Therefore,

$$f_{Tw}(Q = 0; \lambda_{[\underline{T}, \bar{T}]}) + f_{Tw}(Q \neq 0; \lambda_{[\underline{T}, \bar{T}]}) \cdot \int f_{TQ} [T, Q; Q \neq 0, R(t)] dT dQ = 1. \tag{36}$$